Heterogeneous Optical Access Networks: Enabling Low-Latency 5G Services with a Silicon Photonic Smart Edge

Xun Guan, Raphaël Dubé-Demers, Wei Shi, and Leslie A. Rusch

Heterogeneous Optical Access Networks: Enabling Low-Latency 5G Services with a Silicon Photonic Smart Edge

Xun Guan, *Member, IEEE,* Raphaël Dubé-Demers, Wei Shi, *Senior Member, IEEE,* and
Leslie A. Rusch, *Fellow, IEEE*

Abstract—In the 5G era, optical fronthaul is a major challenge in meeting growing demand. Edge computation and coordinated multipoint for 5G have stringent requirements for high throughput and low latency, either in single-wavelength or wavelength-division-multiplexing fronthaul. We propose a new silicon photonic solution to deliver 5G services on existing optical access networks with colorless optical network units, such as passive optical networks. The newly added 5G services form a heterogeneous optical access network. Using the existing fiber infrastructure, broadband services coexist with new 5G signals that can densify 5G coverage. The proposed scheme is both wavelength-selective (in the distribution network) and colorless (at the end user site). We use silicon microring modulators to create subcarriers slaved from the broadband service distributed carrier; additional microring modulators generate 5G signals exploiting those subcarriers. We experimentally validated the successful coexistence of 5G signals (various formats) with a broadband signal (various formats).

Index Terms—Optical fiber communication, photonic integrated circuits, silicon photonics, radio-over-fiber, fronthaul.

I. INTRODUCTION

Fifth generation (5G) mobile communications are a tremendous advance in telecommunication technologies, currently being rolled-out commercially. Optical access networks (OAN) are a key element in the ubiquitous network solution, and must evolve quickly to support further 5G deployment. The OAN must have high throughput, low latency, low power consumption, and scalability; to exploit existing fiber infrastructure they must be compatible with legacy systems, such as colorless operation. There is much research effort underway to address the challenges that 5G impose on an OAN [1]–[3].

Low cost is a stringent requirement for such OANs, both in terms of capital expense (CAPEX), such as construction cost in upgrading to 5G, and operational expense (OPEX) [4]. To reduce CAPEX, we propose the exploitation of legacy deployed fiber networks when available. For OPEX reduction, we propose the use of new silicon photonics (SiP) technologies.

We propose to exploit deployed fiber infrastructure to accommodate use of multi-access edge computing (MEC) [5], and coordinated multipoint (CoMP) [6], [7] increase 5G network performance in terms of capacity and user experience. Latency requirements are critical both for emerging

applications supported by MEC, and for CoMP to achieve 5G capacity enhancements. The fundamental latency caused by the physical length of optical fiber must be kept short given signal processing delays by software and hardware. A 20 km fiber leads to a transmission time of 100 μs one-way, and is a reasonable compromise on latency and coverage. An ultra low latency, as low as 1 ms, is necessary to support applications such as smart transportation, virtual reality (VR), augmented reality (AR), and health care [8].

To meet latency requirements and exploit deployed fiber, we would add a smart edge to the optical distribution portion of the network, as illustrated in Fig. 1 and in extension to our our previous conference reports in [9], [10]. The OAN can take the form of a passive optical network that adopts a smart edge for adding 5G services to the current provision of broadband Internet services. Alternately, it could be any fiber-in-the-loop network offering both digital data and distribution of 5G signals. The fronthaul (from smart edge to antenna site) can be implemented with a digital or analog carriage of 5G signals.

The conventional common public radio interface (CPRI) [11] using digital radio-over-fiber cannot meet projected 5G fronthaul traffic levels, leading to proposals for new functional splits for CPRI, namely enhanced CPRI (eCPRI) [12]. In eCPRI, part of the baseband signal processing is moved from the baseband unit (BBU) to the remote radio unit (RRU), therefore relieving the fronthaul load between BBU and RRU. This increases the cost and complexity of remote installations, running counter to lowering CAPEX and OPEX, especially as 5G service demand increases, i.e., densification.

Unlike the digital RoF of CPRI and eCPRI, analog radio-over-fiber (ARoF) has lower bandwidth and greater scalability. The ARoF transmissions maintain the communications bandwidth, without the expansion encountered with the CPRI protocol. Analog RoF avoids the use of complex signal processing units at the remote site, thus relieving the cost burden on deployment of large numbers of remote units. We demonstrate analog RoF could be overlaid on an existing OAN, coexisting with revenue-producing digital communications.

Cost is clearly reduced as the fiber infrastructure is reused instead of newly deployed. An optical amplifier, if needed, could cover all wavelength-division multiplexing (WDM) channels and would add marginally to the cost of smart edge equipment. The use of analog RoF reduces cost vis-à-vis eCPRI as only simple, low-cost RRHs would be required, and

The authors are with the Department of Electrical and Computer Engineering, Centre d'Optique, Photonique et Laser (COPL), Université Laval, Quebec, QC, G1V 0A6, Canada (e-mail: xun.guan.1@ulaval.ca; raphael.dube-demers.1@ulaval.ca; wei.shi@gel.ulaval.ca; leslie.rusch@gel.ulaval.ca).
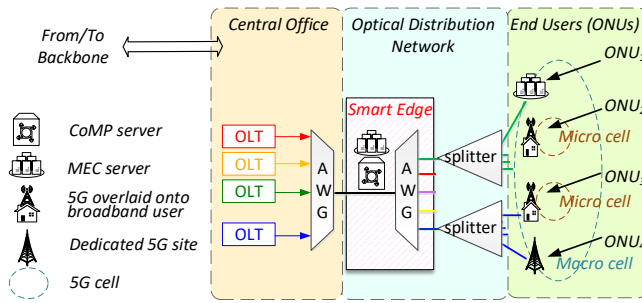
Fig. 1. Schematic view of WDM-OAN in 5G

subsystems can be implemented in power efficient SiP. The 5G BBUs can meet latency requirement as the smart edge located at a remote node would be close to RRHs.

Last but not least, we propose the use of SiP whose merits include its compatibility with complementary metal–oxide–semiconductors (CMOS) technology, its high integration of functional blocks and its low-cost and high-quality silicon-on-insulator (SoI) wafers [13]. SiP has been envisioned to play important roles in optical-wireless convergence [14], [15]. These attributes are essential in enabling heterogeneous services.

From a system perspective, we seek SiP solutions that provide colorless devices and (to future-proof this solution) subsystems compatible with WDM. Among the SiP arsenal of modulation devices, the microring modulator (MRM) stands out for this application. The MRM is extremely small in size, so that incremental optical loss is small as we add them to cover more WDM channels. Their small size means they inherently consume low power, tending to reduce OPEX. Power consumption on the order of fetmojoules per bit [16] has been demonstrated using diminutive microring modulators. This SiP solution offers good scalability as multiple WDM channels can be covered simply by cascading subsystems for each WDM slot with negligible incremental loss.

This paper is organized as follows. Section II introduces the principle of delivering 5G services in a WDM-OAN with a smart edge. Section III briefly introduces the proposed smart edge realized by cascaded MRMs. Section IV discusses the characterization of MRM, including the bias point and the heating condition. Section V elaborates on our experimental findings from the fabricated chip. We confirm its feasibility with different OAN structures. In section VI a further discussion on MRM is given. Section VII concludes the paper.

II. 5G OVERLAY AT THE SMART EDGE OF A WDM-OAN

While currently deployed PONs are single wavelength, meeting growing capacity demands will require a move to WDM. A WDM upgrade would replace passive splitters at the remote node with an arrayed waveguide grating (AWG). To support heterogeneous services the remote node could house the smart edge for 5G, including a MEC server and a CoMP server. Digital backhaul for 5G could be provided by the PON digital services. Some 5G traffic would be strictly local with processing by the MEC.

The WDM-OAN for 5G depicted in Fig. 1 was adapted from a typical passive optical network (PON) [17]. The central office (CO) works as both the interface to the backbone network, and the control center for the WDM-OAN. The CO consists of multiple optical line terminals (OLT) working at different wavelengths, which are combined with an AWG. A single fiber supporting the WDM link connects the CO to a remote node/smart edge. An AWG distributes wavelengths to subscribers. Power splitters could again be used to distribute time multiplexed signals to multiple PON subscribers on a given wavelength.

A. Usage scenarios

With the introduction of 5G signals at the smart edge, several types of end user could be supported. In addition to broadband residential services, micro cells and macro cells could be serviced by optical network units (ONU). Simple optical to electrical conversion at the ONU RRH would generate wireless signals, either in baseband or already on the wireless carrier. Simple RRH hardware would connect these signals to antennas to serve the 5G end users. The 5G RRH could be collocated with a broadband subscriber, or a subscription line could be dedicated to an RRH.

Four ONUs are shown, representing three typical cases: ONU_1 includes a MEC server which enables edge computing for computing intensive applications; ONU_2 and ONU_3 overlay 5G services to broadband services, in different WDM channels; ONU_4 is an RRU which is fully operated by mobile network operators (i.e., no residential client broadband signal).

The smart edge accommodates 5G services in addition to the original broadband services at ONU_2. As the smart edge is connected to all ONUs, it enables the pooling of all channel state information (CSI) among BBUs. Multiple overlapping cells, for instance, ONU_2 and ONU_4, could use CoMP to reduce interference and increase capacity. The smart edge MEC supporting applications could be further optimized by coordination with BBUs (e.g., sharing unused processing units). Also, the remote MEC server at ONU_1 is accessible to ONU_2, ONU_3 and ONU_4, at the smart edge. This paradigm expands available resources for edge computing, reduces latency, and allows the evolution from mobile edge computing to multi-access computing by taking advantage of fixed access facilities [18].

B. Spectrum management

We present the spectral allocations for the overlay and the evolution of spectral content along the OAN as insets to Fig. 2. The broadband downlink service is delivered by a distributed carrier (red arrow) with single-side band (SSB) modulation (hashed red rectangle). The choice of SSB modulation for next generation PONs is essential if modulation rates are to grow while conserving direct detection [19]–[21]; power fading induced by chromatic dispersion precludes high rate baseband transmissions. The SSB modulation also improves the spectral efficiency and combats Rayleigh backscattering interference [22].
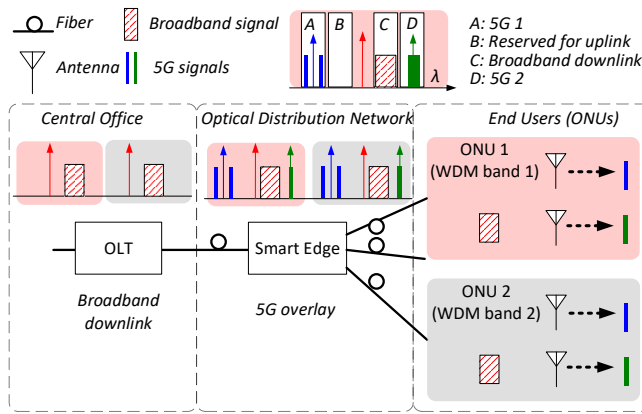
Fig. 2. Smart Edge in WDM-OAN

Each WDM band is subdivided and the distributed carrier is used to seed new subcarriers. Two WDM bands are illustrated in Fig. 2, each having two new subcarriers modulated by 5G signals destined for delivery to remote antennas. The upper inset identifies various sections of a WDM band. The broadband SSB broadband signal is in subband C, and subband B is reserved for the broadband uplink [23]. Two remaining subbands support 5G services overlay, denoted as A and D. The baseband 5G example in subband D would require an electrical mixer at the RRH to bring it to the carrier frequency. The radio frequency over fiber signal in subband A only requires optical to electrical conversion and could be attractive for high frequency 5G signals.

C. Backward compatibility

Current OANs on a single wavelength use OOK or PAM modulation. Our proposed solution is backward compatible due to the wavelength-selectivity in the smart edge. The legacy wavelength could be left untouched and original ONU traffic could pass unaffected; hardware and software upgrade would be unnecessary at those ONUs.

As WDM is rolled out and higher bit rates are favored, a subcarrier multiplexed solution with SSB becomes favorable. Legacy OOK and PAM with double side band (DSB) modulations will suffer severely from fading due to chromatic dispersion [24] as baud rates increase. For these new WDM channels, we propose the overlay of 5G services. The proposed scheme utilizes the conventional trunk fiber, infrastructures and existing facilities (central office and remote-node stations), preserves the legacy ONU, and exploits new high-bandwidth broadband ONU to co-exist with new 5G services.

III. A Smart-Edge Using SiP subsystems

The overlay of 5G service in one WDM band involves two functions: the generation of a subcarrier to carry the 5G signals, and 5G signal modulation. Our silicon photonics subsystems for each function exploit microring modulators (MRMs). MRMs are both wavelength-selective (via thermal tuning) and colorless (they can be tuned across a very wide band) and thus versatile building blocks.

A. MRM bus

Consider a linear cascade of MRMs on a bus. As a resonant device, each MRM only modulates a specific wavelength, passing on other wavelengths with negligible losses. The resonance wavelength of the MRM can be thermally tuned by integrated heaters. In comparison, Mach-Zehnder modulators (MZMs) have much larger footprints [25], [26] an can not be used in a cascaded structure; the much more complex routing and signal combining would incur greater losses than our MRM solution.

The MRM is unrivaled for small footprint and low power consumption (femtojoule) [16]. As a result, the smart edge devices could be small even when covering a large number of WDM bands, and power consumption would remain reasonable. We note that the AWG following the smart edge could be easily integrated with the MRM cascade [27].
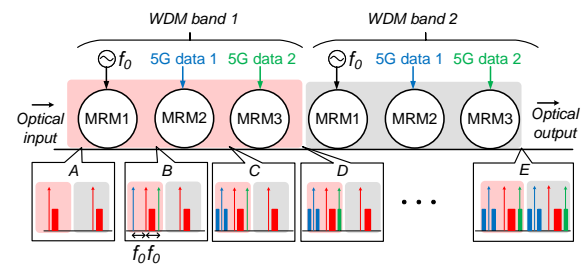

Fig. 3. Principle of smart edge based on cascaded MRM

Fig. 3 shows the principle of operation of the MRM cascade. For our example, a group of three MRMs service each WDM band. In WDM band 1, MRM1 generates the subcarriers by modulating the main carrier with a clock source at f_0. This allows for programmable subcarrier spacing. We examine two subcarriers, but multiple tone generation has also been demonstrated [28]. The subcarriers are used by MRM2 and MRM3 to generate optical versions of the 5G signals. The insets A through D depict the spectra in this process.

After WDM band 1, the optical signal continues to the next group of MRMs. The WDM band 1 signals are unchanged by remaining MRMs as they fall outside their passband. The next group of three MRMs are tuned for WDM band 2. The same RF source could be used to generate the subcarriers in this WDM band. Each group of MRMs in turn would be tuned to the targeted WDM band; if unneeded, they could simply be tuned away from any occupied bands. The spectrum after two WDM bands is shown in inset E. The next step would be an AWG to distribute the WDM bands to various ONUs.

B. MRM Design and Characterization

We designed a chip for the proposed scheme using all-pass MRMs exploiting carrier-depletion PN diodes [16], [29]. The layout of a single MRM is shown in Fig. 4a. The metal heater covered 95% of the ring waveguide circumference and is not shown. The straight waveguide and ring waveguide had a width of $0.5\,\mu m$, and height of $0.22\,\mu m$. The ring waveguide radius was $10\,\mu m$, while the gap between ring waveguide and straight waveguide was $0.315\,\mu m$. There were three doping
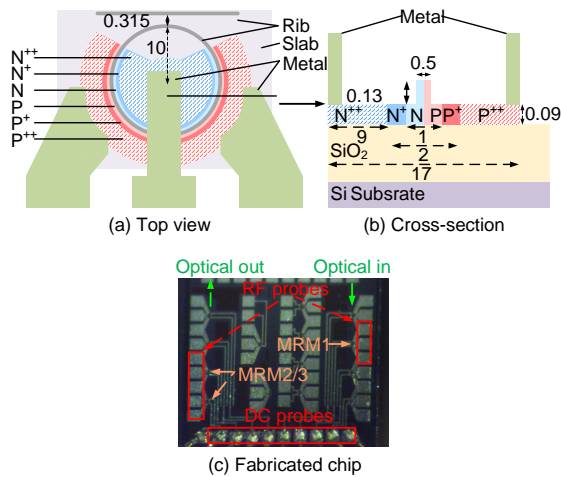
Fig. 4. MRM design and fabrication (unit: μm)
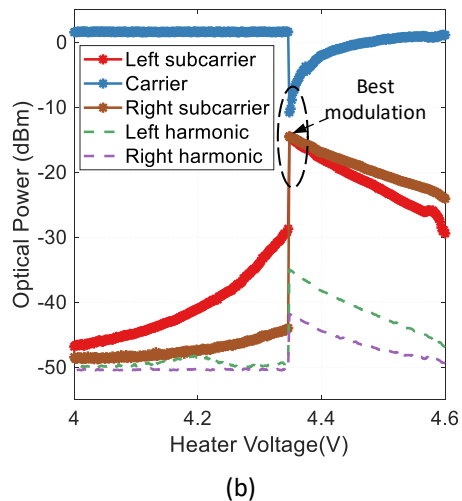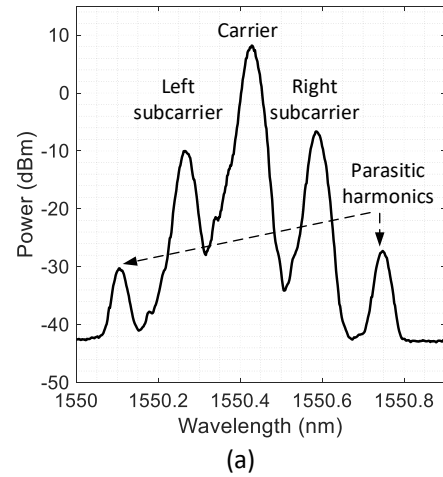

Fig. 5. For reverse bias at $-2\,\text{V}$, (a) spectrum after subcarrier generation, and (b) power of peaks as MRM is thermally tuned.

concentrations in both P and N. A $0.09\,\mu\text{m}$ silicon slab was used for the high-density doping and the metal contact. The cross-section view in Fig. 4b indicates dimensions of various sections. The design was fabricated within a multiple project wafer at IME, A*STAR, Singapore. A photo of the fabricated chip is shown in Fig. 4c. The modulation bandwidth and characteristics could be found in [28].

IV. SUBCARRIER GENERATION

We conducted experiments to study the bias and heating conditions of a MRM for the subcarrier generation. We modulated the optical carrier with a radio frequency (RF) signal of $20\,\text{GHz}$. Figure 5a shows a typical spectrum after modulation measured with an optical spectrum analyzer (OSA, Ando 6317B), with a laser (carrier) at $1550.42\,\text{nm}$ and a reverse bias at $-2\,\text{V}$. The MRM was tuned for resonance at $1550.46\,\text{nm}$. The two subcarriers were produced at $1550.28\,\text{nm}$ and $1550.58\,\text{nm}$. It should be noted that due to the OSA resolution the figure does not show the laser linewidth and the power levels of tone and noise precisely.

The spectrum in Fig. 5a shows three prominent tones: the original carrier and two subcarriers $20\,\text{GHz}$ to either side. Two additional tones at lower power represented parasitic harmonics at a frequency offset of $40\,\text{GHz}$ from the carrier. When tuning MRM1 via the heater voltage, the peak values in the spectrum changed. In Fig. 5b we show the peak power of each tone as we sweep heater voltage.

The carrier-to-subcarrier ratio was the power of the distributed carrier divided by the power of a subcarrier. It varied with the resonant frequency of the MRM accomplished by applying voltage to the MRM heater. The parasitic harmonics were caused by nonlinearity in the MRM response. They were undesirable not only for leaching out power, but also for causing interference when it overlapped with adjacent WDM bands. We could use the heater to find the targeted carrier-to-subcarrier ratio, with the lowest value (most power transferred to subcarriers) occurring at $1550.42\,\text{nm}$.

Fig. 5 reports results from our experiment where we initiated the heater voltage at $4.6\,\text{V}$ and lowered it gradually to $4\,\text{V}$,

with a step size of $0.002\,\text{V}$. Decreasing the heater voltage introduced a temperature drop and blue-shift, thus shifting the MRM transmission spectrum to the left. As we approached a voltage of $4.34\,\text{V}$, the modulation depth of the MRM increased and power moved from the distributed carrier to the subcarriers. After passing the extreme resonance point, the modulation depth decreased abruptly.

The asymmetry at the dip was due to the MRM self-heating effect [30]. As we passed below $4.34\,\text{V}$ while blue-shifting the MRM resonance, more power entered the MRM and enhanced the self-heating effect.

This led to a red-shift (shifting the MRM transmission spectrum to the right) of the MRM resonance, counteracting the influence of continuing to decrease the heater voltage. The slope approaching the resonance from higher heater voltages was gradual, while from lower voltages it was sharp and forms a bi-stability for sufficiently high input power. At the slope discontinuity we had the greatest transfer of power from distributed carrier to subcarriers (best modulation as circled in the figure).

With a $20\,\text{GHz}$ $5\,\text{V}_{\text{PP}}$ modulation, an exhaustive search was conducted to study the best operating point of the MRM
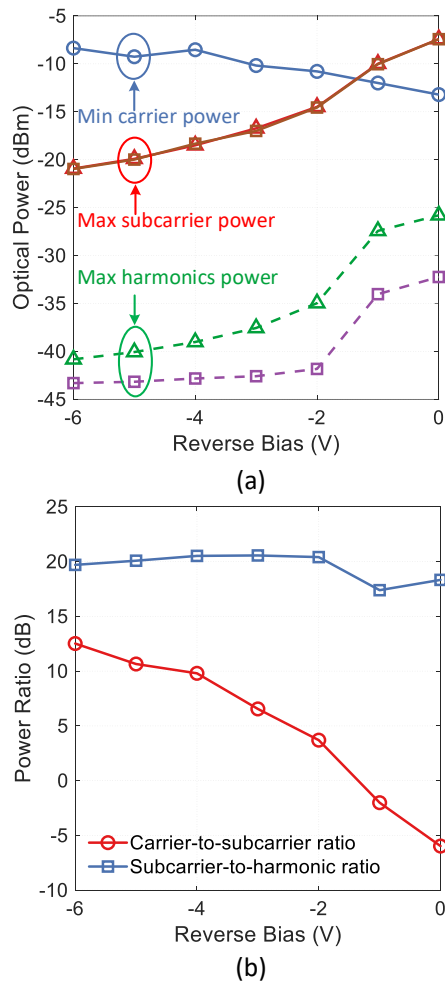
Fig. 6. Dependence on reverse bias at resonance for (a) carrier, subcarriers and harmonics, and (b) carrier-to-subcarrier and subcarrier-to-harmonic power ratios.

for subcarrier generation with regard to reverse bias voltages, varying from -6 V to zero in 1 V steps. With each reverse bias, we captured a trace such as that in Fig. 5b. From these plots we recorded subcarrier powers at the heater setting where carrier power is at a minimum; subcarrier power was maximized when the carrier power was minimized as harmonic power was much lower that subcarrier power. The results were presented in Fig. 6a; note that subcarrier powers were nearly identical, hence the curves were superimposed. The lines show the optimal working point of MRM by generating the highest subcarriers. As the reverse bias voltage approached zero, the majority of power shifted to the subcarriers; the detrimental harmonics increased at a similar rate, but remained relatively small. The carrier-to-subcarrier ratio, and subcarrier-to-harmonic are given in Fig. 6b. The carrier-to-subcarrier ratio dropped to 0 dB at about -1.5 V, indicating a flat comb. The subcarrier-to-harmonic ratio stayed relatively constant, with a slight rise when the reverse bias rose above -2 V.

V. TRANSMISSION EXPERIMENTS

We report experimental evidence that the SiP subsystems can overlay 5G analog radio-over-fiber signals on pre-existing downlink very wideband digital data signals. We receive each signal - the original digital signal and two types of analog RoF signals - and confirm the good performance of each.

A. Experimental setup

We studied the performance of the fabricated chip using the experimental setup in Fig. 7. Our OLT is two lasers (CoBrite DX1) to emulate WDM C-band tones at 100 GHz separation: 1537.792 nm (WDM band 1) and 1538.581 nm (WDM band 2). We reserve half the laser power for carriers, and the other half was modulated by an IQ modulator to generate an SSB signal. A 64 GS/s digital-to-analog converter (DAC) produced the wideband digital signal. This downlink WDM signal was transmitted on 20 km single-mode fiber (SMF) to emulate the OAN trunk fiber.

The smart edge is our SiP unpackaged chip. Input and output fiber arrays were glued to chip grating couplers, with a total 12 dB loss. We compensate these losses with EDFA1. We drove the first MRM (MRM1) with a 20 GHz clock from a signal synthesizer (Anritsu MG3694C), producing two subcarriers. MRM1 was biased at 0 V, see section IV, while MRM2 and MRM3 were biased at -2 V. We used on-chip heaters to tune the MRM operating points. The smart edge signal was transmitted over 5 km SMF emulating the feeder fiber. We use EDFA2 to complete compensation of loss, as EDFA1 gain was limited to 8 dB.

A true ONU would receive all signals in independent photodetectors, such as those implemented in SiP and demonstrated in [23]. For our ONU, we used a programmable optical filter (Finisar Waveshaper 4000s) to select the downlink signal to be tested. Our focus is on the smart edge SiP subsystem. We monitored signals with an optical spectrum analyzer (OSA, Apex AP2043B) with resolution of 100 MHz. To sweep the received optical power, we used an EDFA3, a tunable optical filter to reject out-of-band additive spontaneous emission (ASE) noise, and a variable optical attenuator (VOA). We directly detected the signal with a photodiode (Agilent 11982A). Our 80 GSa/s real-time oscilloscope (RTO, Agilent Infiniium 90000) captured signals. We implemented a digital version of each receiver (broadband or 5G) in offline signal processing.

B. Signals generated

We examined two broadband signaling formats, OFDM and Nyquist-shaped subcarrier modulation. The Nyquist-shaped subcarrier modulated (N-SCM) QPSK broadband signal had a symbol rate of 8 Gbaud. Our N-SCM generation resembled the one in [31]. Our raised cosine roll-off factor was 0.1 for pulse shaping. The subcarrier frequency was 0.35 of the symbol rate, thus the N-SCM signal was centered at 6.8 GHz. After removing an FEC overhead of 7%, and an equalizer training overhead of 5.8%, the overall net bit rate was about 14 Gbps. At the receiver side, we use a 10-tap least-mean-square (LMS) for equalization before decision.

The OFDM signal was generated by QPSK modulation of subcarriers from 4.25 GHz to 10.25 GHz, for an occupied bandwidth of 6 GHz and a 4.25 GHz guard band. After
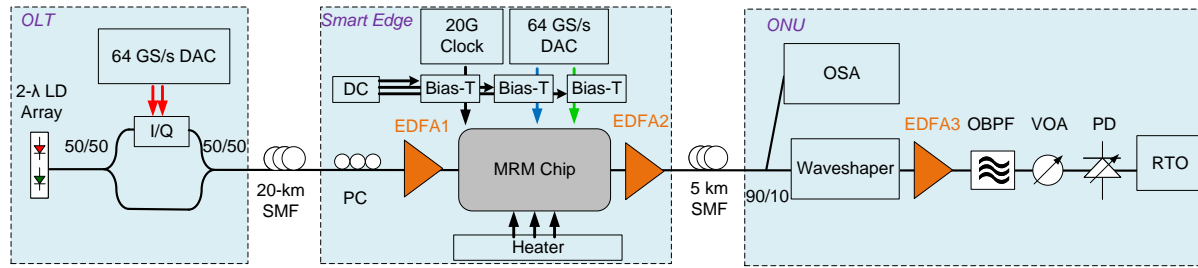
Fig. 7. Experimental setup. LD: laser diode; DAC: digital-to-analog converter; I/Q: IQ modulator; DC: DC power supply; SMF: single-mode fiber; EDFA: erbium-doped fiber amplifier; OSA: optical spectrum analyzer; OBPF: optical bandpass filter; VOA: variable optical attenuator; PD: photodiode; RTO: real-time oscilloscope.

accounting for reasonable overhead for cyclic prefix, training symbols and forward error correction (FEC), the overall net bit rate was about 10 Gbps.

The two 5G signals are QPSK-OFDM throughout our experiments, as a proof-of-concept. Higher modulation formats are possible with more careful optimization of practical issues (loss, modulator characteristics, etc.). We examine both baseband and passband analog RoF signals. The baseband signal would require a local oscillator at RRU; the other could be directly emitted without upconversion. We used a 1 GHz bandwidth for the baseband 5G signal, and a 750 MHz bandwidth with an RF carrier of 3.5 GHz for the passband case. Taking into consideration a hard-decision FEC with 7% overhead, the bit error rate (BER) plots include a FEC threshold line at BER of 3.8×10^{-3}. All 5G signals are OFDM. We used a cyclic prefix and training sequence of 9%, leading to net 5G bit rates of 1.67 Gbps for the baseband RoF and 1.25 Gbps for the passband RoF, respectively, including FEC overhead.

C. Experimental results

In the first experiment, the broadband signal was N-SCM in each WDM band. We overlaid the 5G service alternately in one WDM band. To detect the four signals, we set the waveshaper central wavelength to that of the target signal. In Fig. 8a we show the N-SCM signals from the OLT and in Fig. 8b the addition of subcarriers before their modulation; parasitic harmonics are clear and studied in this series of measurements. The spectra shown in Fig. 8c and d are when adding 5G signals in WDM bands 1 and 2, respectively.

The BER results are presented in Fig. 9. All services could achieve a BER lower than the FEC threshold. Compare 5G performance in Fig. 9a when the 5G signals are overlaid on WDM band 1, and in Fig. 9b for WDM band 2. The performance is unchanged. This demonstrates that the MRM bus of identical modulators can be tuned at will to the targeted WDM band.

Comparing the performance of N-SCM in band 1 in Fig. 9a and b, we again see identical performance. This shows the smart edge interventions did not affect the broadband signal performance. That is, the presence of the parasitic harmonics and the 5G signals did not induce a penalty on N-SCM in WDM band 1.
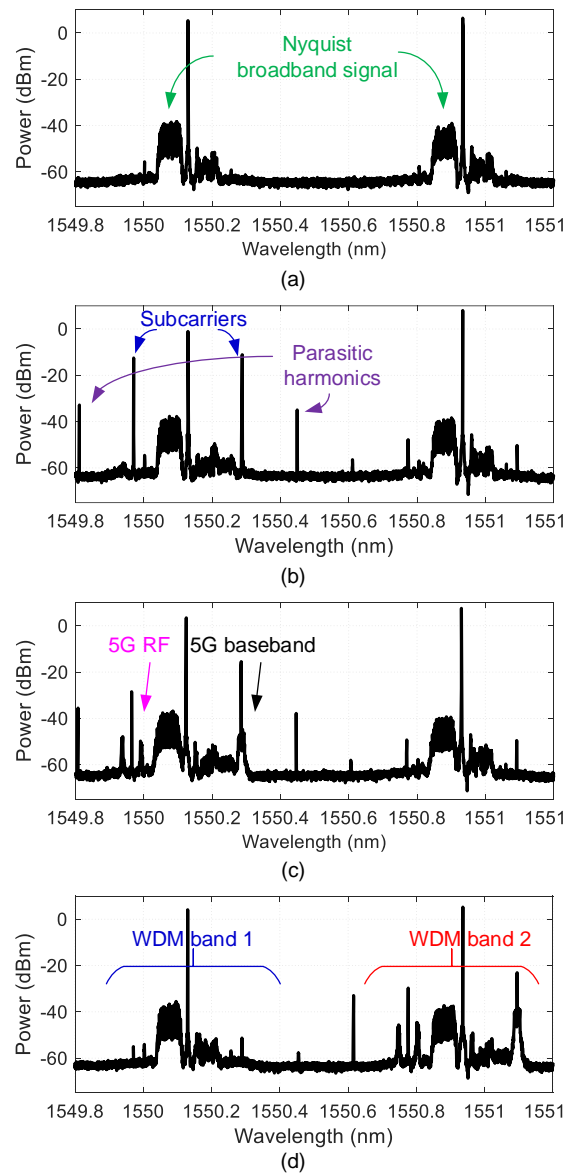

Fig. 8. Optical spectrum with (a) WDM N-SCM broadband signals alone, (b) with subcarriers added in WDM band 1, and for 5G services in (c) WDM band 1, and (d) WDM band 2.
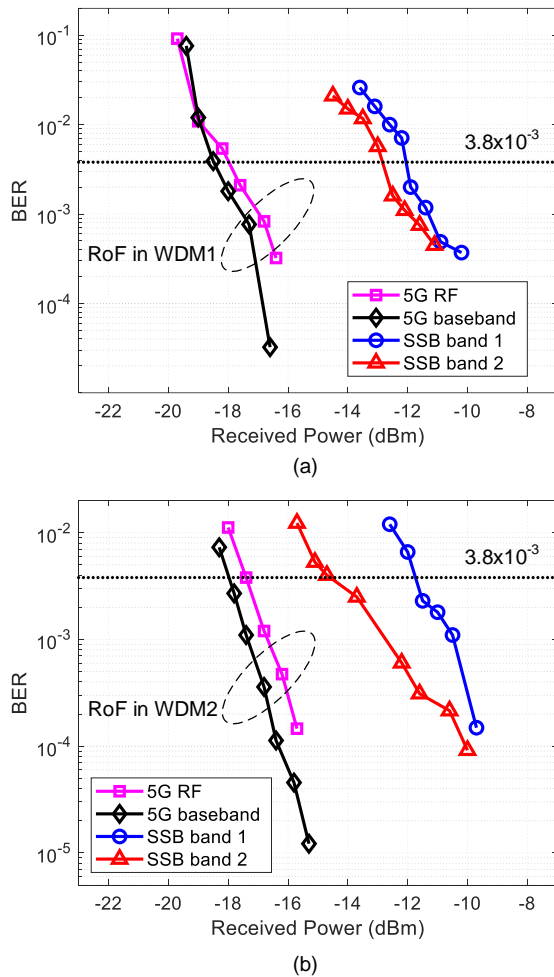
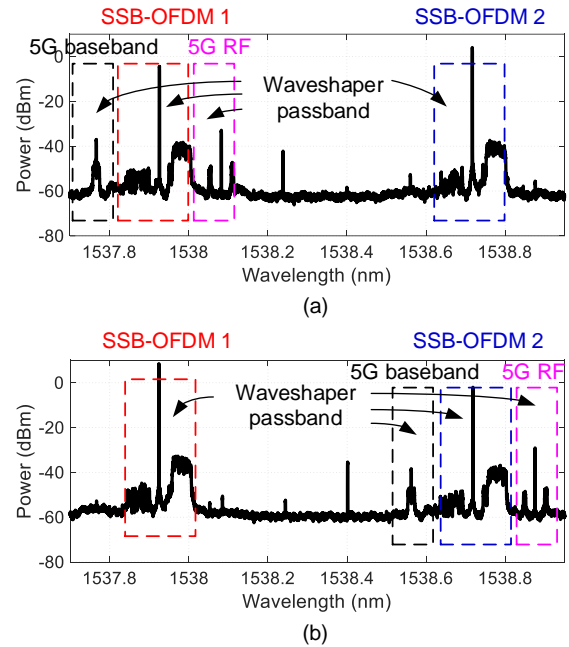Fig. 9. Experimental results of N-SCM broadband signal and 5G signals in (a) WDM band 1, and (b) WDM band 2

Fig. 10. Optical spectrum with WDM SSB-OFDM broadband signals, and for 5G services in (a) WDM band 1, and (b) WDM band 2; dashed boxes are waveshaper settings.

When examining the performance of N-SCM in WDM band 2, however, we do see a penalty at some low received powers. We believe this was induced by some instability in the thermal tuning of the MRM for this experiment. When the MRM drifts, carrier power may decrease, degrading the direct detection of the N-SCM signal. No active feedback was used to stabilize our setup.

Our goal is to examine very high bit rate broadband signals to be deployed in future OANs. Due to the severe impact of chromatic-dispersion-induced fading at these bit rates for baseband optical signals, we only considered subcarrier modulation (OFDM or Nyquist). In our second series of experiments, we replaced the QPSK N-SCM with QPSK-OFDM. The 5G signals were unchanged in this series of measurements.

The spectra are shown in Fig. 10a for placing the 5G signals in WDM band 1, and in Fig. 10b for placing the 5G signals in WDM band 2. We indicate the waveshaper bandwidths and center frequencies in the dashed boxes. The baseband RoF signal is in the black box, and passband RoF signal is in the magenta box.

Fig. 11 shows the BER performance versus received power for all signals. The broadband QPSK SSB-OFDM signals are always present. Consider first Fig. 11a when the 5G signals are overlaid on WDM band 1. The BER for baseband and RF 5G signals, reach below 3.8×10^{-3} at received power of $-18\,\text{dBm}$ and $-16.7\,\text{dBm}$, respectively. For both (WDM1 and WDM2) broadband OFDM signals, the received power for the BER threshold were $-12\,\text{dBm}$, with negligible difference. Hence the overlay does not perturb the principle service provided by the OAN when we introduce the 5G signals.

Next we overlaid the 5G services on WDM band 2 centered at $1538.581\,\text{nm}$, with BER shown in Fig. 11b. Similarly, all four services were detected, demodulated and decoded well below the FEC threshold. The received power for RoF and baseband signal for the BER threshold were $-19\,\text{dBm}$ and $-17.5\,\text{dBm}$, while broadband signal with and without 5G service reached below the threshold at -10 and $-11.5\,\text{dBm}$, respectively. Compared to the previous case, the 5G services outperforms by requiring lower received power for the BER threshold, with the cost of slightly deteriorated performance of the broadband signal with 5G service. This could come from a different working condition of MRM1, with different optical powers transferred from the carrier to subcarriers.

VI. Discussion

A. Proof-of-concept power budget

The presence of three EDFAs in our experimental setup was the result of heavy losses in the setup. Our OLT setup with splitters introduced a 7 dB power loss, while the single-mode fiber and polarization controller contributed 5 dB. This led to low power as we confront the 12 dB coupling loss to the chip (strictly due to working with a bare chip). Due to this extrinsic loss in working with bare chips in the lab environment we introduced EDFA1 ($8\,\text{dB}$ gain). This amplification could be
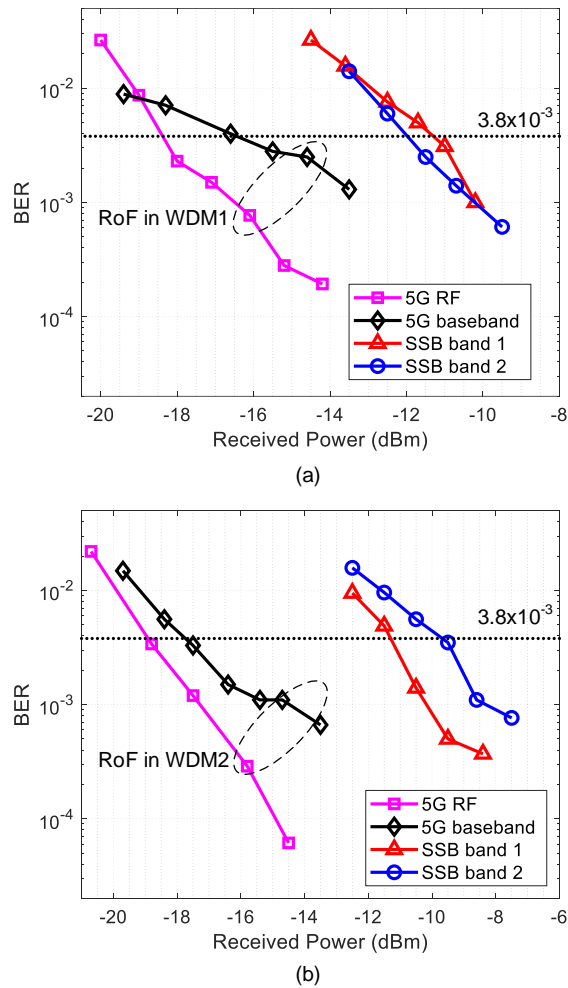
Fig. 11. Experimental results of N-SCM broadband signal and 5G signals in (a) WDM band 1, and (b) WDM band 2.

eliminated with advanced optical packaging technology, which decreases the coupling loss to 1.6 dB [32].

At the ONU side, the waveshaper introduce 8 dB loss and the ASE filter 2 dB loss. The VOA used to adjust the optical power had 5 dB loss (higher than normal). EDFA3 compensated these losses, and guaranteed a tuning range of received power. This EDFA is unnecessary if the waveshaper was replaced with low-loss optical filter technologies, such as integrated microring resonance filters (MRR) [23], especially when using advanced optical packaging. Clearly the VOA and its ASE filter would not be present in a deployed system.

It is not inconceivable that the introduction of a smart edge would perturb the power budget in a deployed OAN and require amplification, such as our EDFA2. However, the cost of adding an EDFA would be small compared to other 5G smart edge equipment. The smart edge introduction leads to the OAN no longer being passive. This deployment is justified not only by servicing a greater number of 5G sites, but more importantly by accommodating a smart edge. The presence of CoMP and MEC servers provides low latency facilities for 5G cooperation and edge computing.

In terms of scalability, the chip insertion losses reflect the largest contribution to the multiple WDM channel case. Supporting more WDM channels by cascading more MRM does not linearly increase total loss. New MRMs does not affect the wavelength that is not modulated [33]. More MRMs only bring a small transmission loss in the waveguide due to the small footprint of MRM, unlike the case of large-footprint silicon Mach Zehnder modulator.

B. Spectrum management

The $10\,\mathrm{um}$-radius MRMs in our experiment had a free spectral range of $10\,\mathrm{nm}$, covering 30% of the C-Band. For initial rollout of WDM PONs, partial C-band coverage may be sufficient. If the entire C-Band is targeted, two strategies are available. One is the modify the MRM for greater FSR, the other is to divide the C-Band into multiple sub-bands covered by the reduced FSR.

The FSR could be increased to $19.5\,\mathrm{nm}$ [29] and beyond by shrinking the radius of MRM, thus covering more wavelengths and avoiding multiple C-band resonances. This approach, however, comes with several disadvantages. Firstly, decreasing the MRM radius, especially below $5\,\mathrm{um}$, increases MRM loss. Secondly, a larger FSR means thermal heater tuning must cover a much greater range. To this challenge is added the higher power consumption coming with greater tuning range. For these reasons, coverage with shorter FSR across multiple sub-bands appears more promising. For instance, we could demultiplex the C-Band into 3 sub-bands each of $10\,\mathrm{nm}$. The demonstrated solution could then be applied by dedicated cascaded MRMs in each sub-band.

We demonstrated two analog RoF signals on two subcarriers, however more subcarriers could be generated by adjusting the RF clock signals. For instance, in the demonstration in [28] the RF clock was changed to move from two subcarriers to four subcarriers. Given that increasing the number of subcarriers requires much more stringent optical filtering and MRM wavelength selectivity, this may not be the best method to scale. Multiple RF signals can be treated as a single MRM drive signal and detected as a unit at the ONU, such as the demonstration in [23] of 5 narrowband RF signals. In this case, greater density (and spectral efficiency) is achieved in the RF domain rather than the optical domain.

C. Thermal effects

Due to the high thermal-optic coefficient of silicon and the small-size resonance structure, the thermal effect of MRM is very significant. For example, the resonance drifts as ambient temperature changes. Numerous contributions have been made on the wavelength lock of MRM, for example in [34]–[36]. In our proposed scheme the thermal effect is especially significant at MRM1 for the subcarrier generation, as the input optical power is high [37]. While our proof-of-concept experiment used an all-pass MRM, deployed systems would be better served with an MRM with a drop waveguide and a on-chip integrated photodiode to monitor and lock the MRM [35].

In section IV we studied the operating point of MRM by exhaustively searching the resonance of the MRM when sweeping reverse biases. Although the best modulation can be
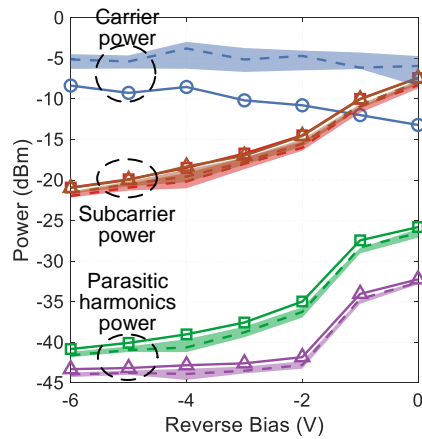
Fig. 12. Power of carrier, subcarriers and harmonic versus reverse bias; solid lines at optimal tuning, dashed lines at $0.02\,\mathrm{V}$ offset, and shaded areas at $\pm 0.01\mathrm{V}$ drift around $0.02\,\mathrm{V}$ offset.

achieved by operating at the heater setting circled in Fig. 5, this setting injects high power into MRM. Due to the very sharp slope on one side, maintaining operation at this point would be exceedingly difficult. Instability would lead to a loss of modulation, as observed in practice.

To guarantee a robust modulation while maintaining a high subcarrier power, the MRM heater could be set at an offset from the heater setting of the optimal modulation point. Such a point could be chosen to avoid instability. After locating the heater setting for the best modulating power of each reverse bias as reported in Fig. 6, we set the heater voltage to be $0.02\,\mathrm{V}$ higher. We plot this second set of operating points for the MRM versus the same reverse bias voltages, shown as dashed lines in Fig. 12. Solid lines repeat the values shown in Fig. 6 for ready comparison. Finally we varied the heater voltage by $\Delta V = \pm 0.01\,V$ around the $0.02\,\mathrm{V}$ offset. These extrema define the shaded areas of power in the figure.

We conclude that an offset from the best modulation allows for a range of variation, with only very small degradation in the power of subcarriers. That is, there is only a moderate increase in the power remaining to the carrier and not transformed into subcarriers. This would accommodate a feedback loop to assure stabilization in future designs, with the help of integrated Ge waveguide photodetector [35].

D. Polarization diversity

We note that the chips designed and used here employed grating couplers. High insertion loss could be avoided with advanced, industrial optical coupling techniques [32], [38]. Grating couplers are also polarization sensitive, which required we use a polarization controller before the smart edge. However, this is not a fundamental limit, as polarization insensitive optical coupling based on edge coupling [39] or two-dimensional grating couplers [40] could alleviate this constraint. With a polarization-insensitive design both polarizations of the optical signal could be coupled into the chip and processed. Coverage of the C-band by grating couplers

has been demonstrated [41], [42]. These shortcomings could be explored in future designs.

VII. CONCLUSION

We have proposed a novel smart edge architecture for 5G delivery, and proposed hardware based on silicon microring modulators. The SiP subsystem provides for both subcarrier generation and signal modulation. The use of SiP and resonant structures keep cost, footprint and power consumption low. The proposed heterogeneous service architecture can work colorlessly in a wavelength division multiplexed optical access network.

We designed and tested the chip following fabrication. Our experimental demonstrations validate the functionality of the proposed scheme, by successfully receiving broadband and 5G signals to a BER level lower than the HD-FEC threshold. By adding ARoF we simplify RRUs, unlike the eCPRI solution that overcome the great bandwidth requirements of digital RoF by pushing complexity to RRUs. Our solution is thus more scalable for cell densification. The proposed smart edge meets latency requirements by shortening the transmission distance of 5G services, and avoiding the queue and signal processing latency of CRPI/eCPRI.

REFERENCES

[1] K. Kim, K.-H. Doo, H. H. Lee, S. Kim, H. Park, J.-Y. Oh, and H. S. Chung, "High speed and low latency passive optical network for 5G wireless systems," *Journal of Lightwave Technology*, vol. 37, no. 12, pp. 2873–2882, 2018.

[2] X. Liu and F. Effenberger, "Emerging optical access network technologies for 5G wireless," *IEEE/OSA Journal of Optical Communications and Networking*, vol. 8, no. 12, pp. B70–B79, 2016.

[3] J. Zhang, Y. Ji, S. Jia, H. Li, X. Yu, and X. Wang, "Reconfigurable optical mobile fronthaul networks for coordinated multipoint transmission and reception in 5G," *IEEE/OSA Journal of Optical Communications and Networking*, vol. 9, no. 6, pp. 489–497, 2017.

[4] M. Levantesi and D. A. Mlo, "An insight into the total cost of ownership of 5G fronthauling," in *2018 20th International Conference on Transparent Optical Networks (ICTON)*, pp. 1–5, IEEE, 2018.

[5] T. Taleb, K. Samdanis, B. Mada, H. Flinck, S. Dutta, and D. Sabella, "On multi-access edge computing: A survey of the emerging 5G network edge cloud architecture and orchestration," *IEEE Communications Surveys & Tutorials*, vol. 19, no. 3, pp. 1657–1681, 2017.

[6] V. Jungnickel, K. Manolakis, W. Zirwas, B. Panzner, V. Braun, M. Lossow, M. Sternad, R. Apelfröjd, and T. Svensson, "The role of small cells, coordinated multipoint, and massive mimo in 5g," *IEEE communications magazine*, vol. 52, no. 5, pp. 44–51, 2014.

[7] A. Checko, H. L. Christiansen, Y. Yan, L. Scolari, G. Kardaras, M. S. Berger, and L. Dittmann, "Cloud RAN for mobile networks—a technology overview," *IEEE Communications surveys & tutorials*, vol. 17, no. 1, pp. 405–426, 2014.

[8] I. Parvez, A. Rahmati, I. Guvenc, A. I. Sarwat, and H. Dai, "A survey on low latency towards 5G: RAN, core network and caching solutions," *IEEE Communications Surveys & Tutorials*, vol. 20, no. 4, pp. 3098–3130, 2018.

[9] X. Guan, Y. Xu, J. Lin, M. Lyu, R. Dubé-Demers, S. LaRochelle, W. Shi, and L. A. Rusch, "Enabling 5G services in PON with a novel smart edge based on SiP MRM," in *Optical Fiber Communication Conference*, pp. Th3G–3, Optical Society of America, 2018.

[10] X. Guan, R. Dubé-Demers, W. Shi, and L. A. Rusch, "5G service overlay in WDM optical access network with colorless smart edge based on SiP MRM," in *Conference on Lasers and Electro-Optics*, p. STu4L.3, Optical Society of America, 2020.

[11] C. Specification, "V6. 1," *Common public radio interface (CPRI)*, 2014.

[12] J. S. Wey and J. Zhang, "Passive optical networks for 5G transport: technology and standards," *Journal of Lightwave Technology*, vol. 37, no. 12, pp. 2830–2837, 2018.

[13] D. Thomson, A. Zilkie, J. E. Bowers, T. Komljenovic, G. T. Reed, L. Vivien, D. Marris-Morini, E. Cassan, L. Virot, J.-M. Fédéli, *et al.*, "Roadmap on silicon photonics," *Journal of Optics*, vol. 18, no. 7, p. 073003, 2016.

[14] K. Van Gasse, J. Van Kerrebrouck, A. Abbasi, G. Torfs, J. Bauwelinck, and G. Roelkens, "16 Gbps RoF link at 20 GHz carrier frequency using a silicon photonics transmitter and receiver," in *2017 International Topical Meeting on Microwave Photonics (MWP)*, pp. 1–4, IEEE, 2017.

[15] Y. Tong, C.-W. Chow, G.-H. Chen, C.-W. Peng, C.-H. Yeh, and H. K. Tsang, "Integrated silicon photonics remote radio frontend (RRF) for single-sideband (SSB) millimeter-wave radio-over-fiber (ROF) systems," *IEEE Photonics Journal*, vol. 11, no. 2, pp. 1–8, 2019.

[16] R. Dubé-Demers, S. LaRochelle, and W. Shi, "Ultrafast pulse-amplitude modulation with a femtojoule silicon photonic modulator," *Optica*, vol. 3, no. 6, pp. 622–627, 2016.

[17] J. Zou, C. Wagner, and M. Eiselt, "Optical fronthauling for 5G mobile: A perspective of passive metro WDM technology," in *2017 Optical Fiber Communications Conference and Exhibition (OFC)*, pp. 1–3, IEEE, 2017.

[18] I. Morris, "ETSI drops 'mobile' from MEC," *Lightreading*, Sep 2016.

[19] K. Yonenaga and N. Takachio, "A fiber chromatic dispersion compensation technique with an optical SSB transmission in optical homodyne detection systems," *IEEE Photonics Technology Letters*, vol. 5, no. 8, pp. 949–951, 1993.

[20] X. Zhang, C. Zhang, C. Chen, W. Jin, and K. Qiu, "Non-optical carrier SSB-OFDM PONs with the improved receiver sensitivity and potential transmission nonlinearity tolerance," *IEEE Photonics Journal*, vol. 9, no. 1, pp. 1–10, 2017.

[21] W. Jin, A. Sankoh, Y. Dong, Z.-Q. Zhong, R. P. Giddings, M. O'Sullivan, J. Lee, T. Durrant, and J. Tang, "Hybrid SSB OFDM-digital filter multiple access pons," *Journal of Lightwave Technology*, vol. 38, no. 8, pp. 2095–2105, 2020.

[22] C.-H. Yeh and C.-W. Chow, "Using single side-band modulation for colorless ofdm-wdm access network to alleviate rayleigh backscattering effects," *Optics express*, vol. 24, no. 10, pp. 10898–10903, 2016.

[23] M. Lyu, W. Shi, and L. A. Rusch, "Silicon photonic subsystem for broadband and RoF detection while enabling carrier reuse," *Optics Express*, vol. 28, no. 10, pp. 14897–14907, 2020.

[24] B. Lin, J. Li, H. Yang, Y. Wan, Y. He, and Z. Chen, "Comparison of DSB and SSB transmission for OFDM-PON," *Journal of Optical Communications and Networking*, vol. 4, no. 11, pp. B94–B100, 2012.

[25] H. Sepehrian, J. Lin, L. A. Rusch, and W. Shi, "Silicon photonic IQ modulators for 400 Gb/s and beyond," *J. Lightwave Technol.*, vol. 37, pp. 3078–3086, Jul 2019.

[26] A. Samani, V. Veerasubramanian, E. El-Fiky, D. Patel, and D. V. Plant, "A silicon photonic PAM-4 modulator based on dual-parallel Mach-Zehnder interferometers," *IEEE Photonics Journal*, vol. 8, no. 1, pp. 1–10, 2015.

[27] S. Pathak, M. Vanslembrouck, P. Dumon, D. Van Thourhout, and W. Bogaerts, "Optimized silicon AWG with flattened spectral response using an MMI aperture," *Journal of Lightwave Technology*, vol. 31, no. 1, pp. 87–93, 2013.

[28] Y. Xu, J. Lin, R. Dubé-Demers, S. LaRochelle, L. Rusch, and W. Shi, "Integrated flexible-grid WDM transmitter using an optical frequency comb in microring modulators," *Optics letters*, vol. 43, no. 7, pp. 1554–1557, 2018.

[29] P. Dong, R. Shafiiha, S. Liao, H. Liang, N.-N. Feng, D. Feng, G. Li, X. Zheng, A. V. Krishnamoorthy, and M. Asghari, "Wavelength-tunable silicon microring modulator," *Optics express*, vol. 18, no. 11, pp. 10941–10946, 2010.

[30] M. J. Shin, Y. Ban, B.-M. Yu, J. Rhim, L. Zimmermann, and W.-Y. Choi, "Parametric characterization of self-heating in depletion-type Si micro-ring modulators," *IEEE Journal of Selected Topics in Quantum Electronics*, vol. 22, no. 6, pp. 116–122, 2016.

[31] M. S. Erkılınc, S. Pachnicke, H. Griesser, B. C. Thomsen, P. Bayvel, and R. I. Killey, "Performance comparison of single-sideband direct detection Nyquist-subcarrier modulation and OFDM," *Journal of Lightwave Technology*, vol. 33, no. 10, pp. 2038–2046, 2015.

[32] N. Lindenmann, G. Balthasar, D. Hillerkuss, R. Schmogrow, M. Jordan, J. Leuthold, W. Freude, and C. Koos, "Photonic wire bonding: a novel concept for chip-scale interconnects," *Optics express*, vol. 20, no. 16, pp. 17667–17677, 2012.

[33] Q. Xu, B. Schmidt, J. Shakya, and M. Lipson, "Cascaded silicon micro-ring modulators for WDM optical interconnection," *Optics express*, vol. 14, no. 20, pp. 9431–9436, 2006.

[34] K. Padmaraju, J. Chan, L. Chen, M. Lipson, and K. Bergman, "Thermal stabilization of a microring modulator using feedback control," *Optics express*, vol. 20, no. 27, pp. 27999–28008, 2012.

[35] X. Zheng, E. Chang, P. Amberg, I. Shubin, J. Lexau, F. Liu, H. Thacker, S. S. Djordjevic, S. Lin, Y. Luo, *et al.*, "A high-speed, tunable silicon photonic ring modulator integrated with ultra-efficient active wavelength control," *Optics express*, vol. 22, no. 10, pp. 12628–12633, 2014.

[36] Y. Li and A. W. Poon, "Active resonance wavelength stabilization for silicon microring resonators with an in-resonator defect-state-absorption-based photodetector," *Optics express*, vol. 23, no. 1, pp. 360–372, 2015.

[37] Q. Li, N. Ophir, L. Xu, K. Padmaraju, L. Chen, M. Lipson, and K. Bergman, "Experimental characterization of the optical-power upper bound in a silicon microring modulator," in *2012 Optical Interconnects Conference*, pp. 38–39, IEEE, 2012.

[38] R. Dangel, A. La Porta, D. Jubin, F. Horst, N. Meier, M. Seifried, and B. J. Offrein, "Polymer waveguides enabling scalable low-loss adiabatic optical coupling for silicon photonics," *IEEE Journal of Selected Topics in Quantum Electronics*, vol. 24, no. 4, pp. 1–11, 2018.

[39] D. Dai and H. Wu, "Realization of a compact polarization splitter-rotator on silicon," *Optics letters*, vol. 41, no. 10, pp. 2346–2349, 2016.

[40] D. Taillaert, H. Chong, P. I. Borel, L. H. Frandsen, R. M. De La Rue, and R. Baets, "A compact two-dimensional grating coupler used as a polarization splitter," *IEEE Photonics Technology Letters*, vol. 15, no. 9, pp. 1249–1251, 2003.

[41] Y. Xue, H. Chen, Y. Bao, J. Dong, and X. Zhang, "Two-dimensional silicon photonic grating coupler with low polarization-dependent loss and high tolerance," *Optics express*, vol. 27, no. 16, pp. 22268–22274, 2019.

[42] D. Fowler, P. Grosse, F. Gays, B. Szelag, C. Baudot, N. Vuillet, J. Planchot, and F. Boeuf, "Fiber grating coupler development for Si-photonics process design kits at CEA-LETI," in *Smart Photonic and Optoelectronic Integrated Circuits XXI*, vol. 10922, p. 1092205, International Society for Optics and Photonics, 2019.